Evidence for two-dimensional Ising superconductivity in gated MoS2

Lu, J. M.; Zheliuk, O.; Leermakers, I.; Yuan, N. F. Q.; Zeitler, U.; Law, K. T.; Ye, J. T.

Published in:
Science

DOI:
10.1126/science.aab2277

Publication date:
2015

SUPERCONDUCTIVITY

Evidence for two-dimensional Ising superconductivity in gated MoS_2

J. M. Lu,[1] O. Zheliuk,[1] I. Leermakers,[2] N. F. Q. Yuan,[3] U. Zeitler,[2] K. T. Law,[3] J. T. Ye[1]*

The Zeeman effect, which is usually detrimental to superconductivity, can be strongly protective when an effective Zeeman field from intrinsic spin-orbit coupling locks the spins of Cooper pairs in a direction orthogonal to an external magnetic field. We performed magnetotransport experiments with ionic-gated molybdenum disulfide transistors, in which gating prepared individual superconducting states with different carrier dopings, and measured an in-plane critical field B_{c2} far beyond the Pauli paramagnetic limit, consistent with Zeeman-protected superconductivity. The gating-enhanced B_{c2} is more than an order of magnitude larger than it is in the bulk superconducting phases, where the effective Zeeman field is weakened by interlayer coupling. Our study provides experimental evidence of an Ising superconductor, in which spins of the pairing electrons are strongly pinned by an effective Zeeman field.

In conventional superconductors, applying a sufficiently high magnetic field above the upper critical field B_{c2} is a direct way to destroy superconductivity by breaking Cooper pairs via the coexisting orbital and Pauli paramagnetic mechanisms. The orbital contribution originates from the coupling between the magnetic field and the electron momentum, whereas the paramagnetic contribution is caused by spin alignment in Cooper pairs by an external magnetic field. When the orbital effect is weakened or eliminated, either by having a large electron mass (*1*) or by reducing dimensionality (*2*), B_{c2} is solely determined by the interaction between the magnetic field and the spin degree of freedom of the Cooper pairs. In superconductors where Cooper pairs are formed by electrons with opposite spins, aligning the electron spins by the external magnetic field increases the energy of the system; therefore, B_{c2} cannot exceed the Clogston-Chandrasekhar limit (*3*, *4*) or the Pauli paramagnetic limit (in units of tesla), $B_p \approx 1.86\ T_c(0)$. Here, $T_c(0)$ is the zero-field superconducting critical temperature (in units of kelvin) that characterizes the binding energy of a Cooper pair, which competes with the Zeeman splitting energy.

However, in some superconductors, the Pauli limit can be surpassed. For example, forming Fulde-Ferrell-Larkin-Ovchinnikov states with inhomogeneous pairing densities favors the presence of a magnetic field, even above B_p (*5*). In spin-triplet superconductors, the parallel-aligned spin configuration in Cooper pairs is not affected by Pauli paramagentism, and B_{c2} can easily exceed B_p (*6*–*8*). Spin-orbit interactions have also been shown to align spins to overcome the Pauli limit. Rashba spin-orbit coupling (SOC) in noncentrosymmetric superconductors will lock the spin to the in-plane direction, which can greatly enhance the out-of-plane B_{c2} (*9*); however, for an in-plane magnetic field, B_{c2} can only be moderately enhanced to $\sqrt{2}\,B_p$ (*10*). Alternatively, electron spins can be randomized by spin-orbit scattering (SOS), which weakens the effect of spin paramagnetism (*11*–*15*) and hence enhances B_{c2}.

Superconductivity in thin flakes of MoS_2 can be induced electrostatically using the electric field effect, mediated by moving ions in a voltage-biased ionic liquid placed on top of the sample [section 1 of (*16*); (*17*)]. Negative carriers (electrons) are induced by accumulating cations above the outermost layer of an MoS_2 flake, forming a capacitor ~1 nm thick (*17*–*22*). The potential gradient at the surface creates a planar homogenous electronic system

[1]Device Physics of Complex Materials, Zernike Institute for Advanced Materials, Nijenborgh 4, 9747 AG, Groningen, Netherlands. [2]High Field Magnet Laboratory, European Magnetic Field Laboratory (HFML-EMFL), and Institute of Molecules and Materials, Radboud University, Toernooiveld 7, 6525 ED Nijmegen, Netherlands. [3]Department of Physics, Hong Kong University of Science and Technology, Clear Water Bay, Hong Kong, China.
*Corresponding author. E-mail: j.ye@rug.nl

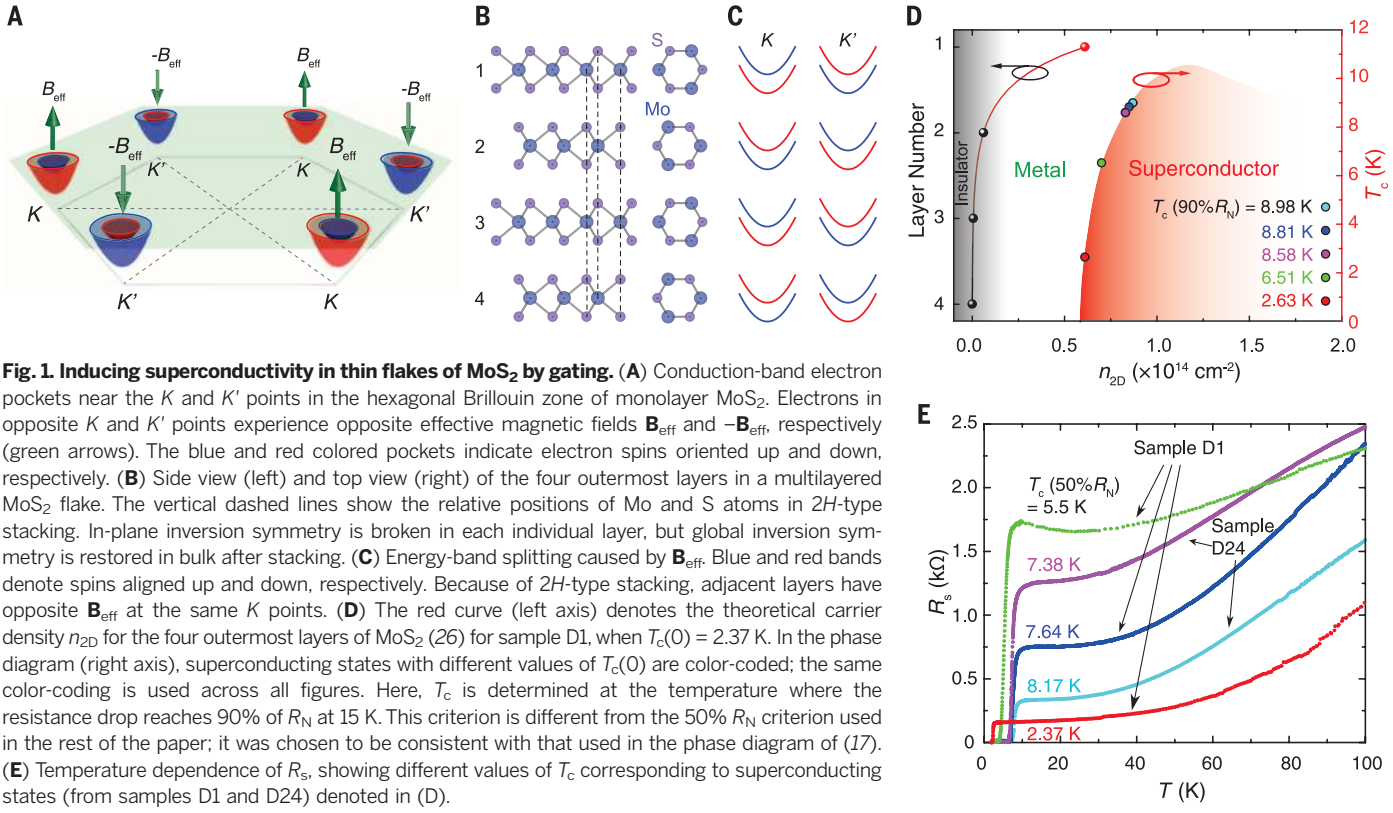

Fig. 1. Inducing superconductivity in thin flakes of MoS_2 by gating. (**A**) Conduction-band electron pockets near the *K* and *K*′ points in the hexagonal Brillouin zone of monolayer MoS_2. Electrons in opposite *K* and *K*′ points experience opposite effective magnetic fields $\mathbf{B}_{eff}$ and $-\mathbf{B}_{eff}$, respectively (green arrows). The blue and red colored pockets indicate electron spins oriented up and down, respectively. (**B**) Side view (left) and top view (right) of the four outermost layers in a multilayered MoS_2 flake. The vertical dashed lines show the relative positions of Mo and S atoms in 2*H*-type stacking. In-plane inversion symmetry is broken in each individual layer, but global inversion symmetry is restored in bulk after stacking. (**C**) Energy-band splitting caused by $\mathbf{B}_{eff}$. Blue and red bands denote spins aligned up and down, respectively. Because of 2*H*-type stacking, adjacent layers have opposite $\mathbf{B}_{eff}$ at the same *K* points. (**D**) The red curve (left axis) denotes the theoretical carrier density n_{2D} for the four outermost layers of MoS_2 (*26*) for sample D1, when $T_c(0) = 2.37$ K. In the phase diagram (right axis), superconducting states with different values of $T_c(0)$ are color-coded; the same color-coding is used across all figures. Here, T_c is determined at the temperature where the resistance drop reaches 90% of R_N at 15 K. This criterion is different from the 50% R_N criterion used in the rest of the paper; it was chosen to be consistent with that used in the phase diagram of (*17*). (**E**) Temperature dependence of R_s, showing different values of T_c corresponding to superconducting states (from samples D1 and D24) denoted in (D).

with an inhomogeneous vertical doping profile, where conducting electrons are predominantly doped into a few of the outermost layers, forming superconducting states near the K and K' valleys of the conduction band (Fig. 1A). The in-plane inversion symmetry breaking in a MoS_2 monolayer can induce SOC, manifested as a Zeeman-like effective magnetic field $\mathbf{B}_{eff}$ (~100 T) oppositely applied at the K and K' points of the Brillouin zone (*23*). Because electrons of opposite momentum experience opposite $\mathbf{B}_{eff}$, this SOC is then compatible with Cooper pairs also residing at the K and K' points (*24*). Therefore, spins of electrons in the Cooper pairs are polarized by this large out-of-plane Zeeman field, which is able to protect their orientation from being realigned by an in-plane magnetic field, leading to a large in-plane B_{c2}. This alternating spin configuration also provides the essential ingredient for establishing an Ising superconductor, where spins of electrons in the Cooper pairs are strongly pinned by an effective Zeeman field in an Ising-like fashion.

Because of the alternating stacking order in 2*H*-type single crystals of transition metal dichalcogenide (TMD) (Fig. 1B), electrons with the same momentum experience $\mathbf{B}_{eff}$ with opposite signs for adjacent layers, which weakens the effect of SOC by cancelling out $\mathbf{B}_{eff}$ mutually in the bulk crystal (Fig. 1C) (a comparison with bulk intercalated TMD is given in section 7 of (*16*)]. However, field-effect doping can strongly confine carriers to the outermost layer, reaching a two-dimensional (2D) carrier density n_{2D} of up to ~10^{14} cm^{-2} (*17*, *25*). Theoretical calculations for our devices indicate that the n_{2D} of individual layers decays exponentially from the channel surface (Fig. 1D, left axis), reducing the n_{2D} of the second-to-outermost layer by almost 90% in comparison with the outermost one (*26*). From the established phase diagram (*17*), if superconductivity is induced close to the quantum critical point (QCP; $n_{2D} \sim 6 \times 10^{13}$ cm^{-2}), the second layer is not even metallic, because metallic transport can be observed only when $n_{2D} > 8 \times 10^{12}$ cm^{-2}. Therefore, the outermost layer is well isolated by gating, mimicking a freestanding monolayer (*27*).

We obtained superconducting states across a range of doping concentrations (Fig. 1D, right axis) by varying the gate voltage (*17*); these states have different temperature dependences of sheet resistivity R_s (Fig. 1E). A superconducting state [T_c (at B = 0) = 2.37 K] at the onset of superconductivity (close to QCP) could be induced without suffering from the inhomogeneity usually encountered at low doping concentrations (Fig. 1E, red curve). Consistently, this well-behaved state also exhibits a high mobility of ~700 cm^2/Vs (measured at T = 15 K) before reaching zero resistance.

Angle-resolved photoemission spectroscopy (ARPES) measurements (*27*, *28*) and theoretical calculations (*25*, *29*) both showed that electron doping starts near the K points of the conduction band. The band structure is modified at higher doping (*25*, *29*), meaning that the simplest superconducting states in MoS_2, which are dominated by Cooper pairs at the K and K' points, should be prepared by minimizing doping [higher doping states are discussed in section 7 of (*16*)].

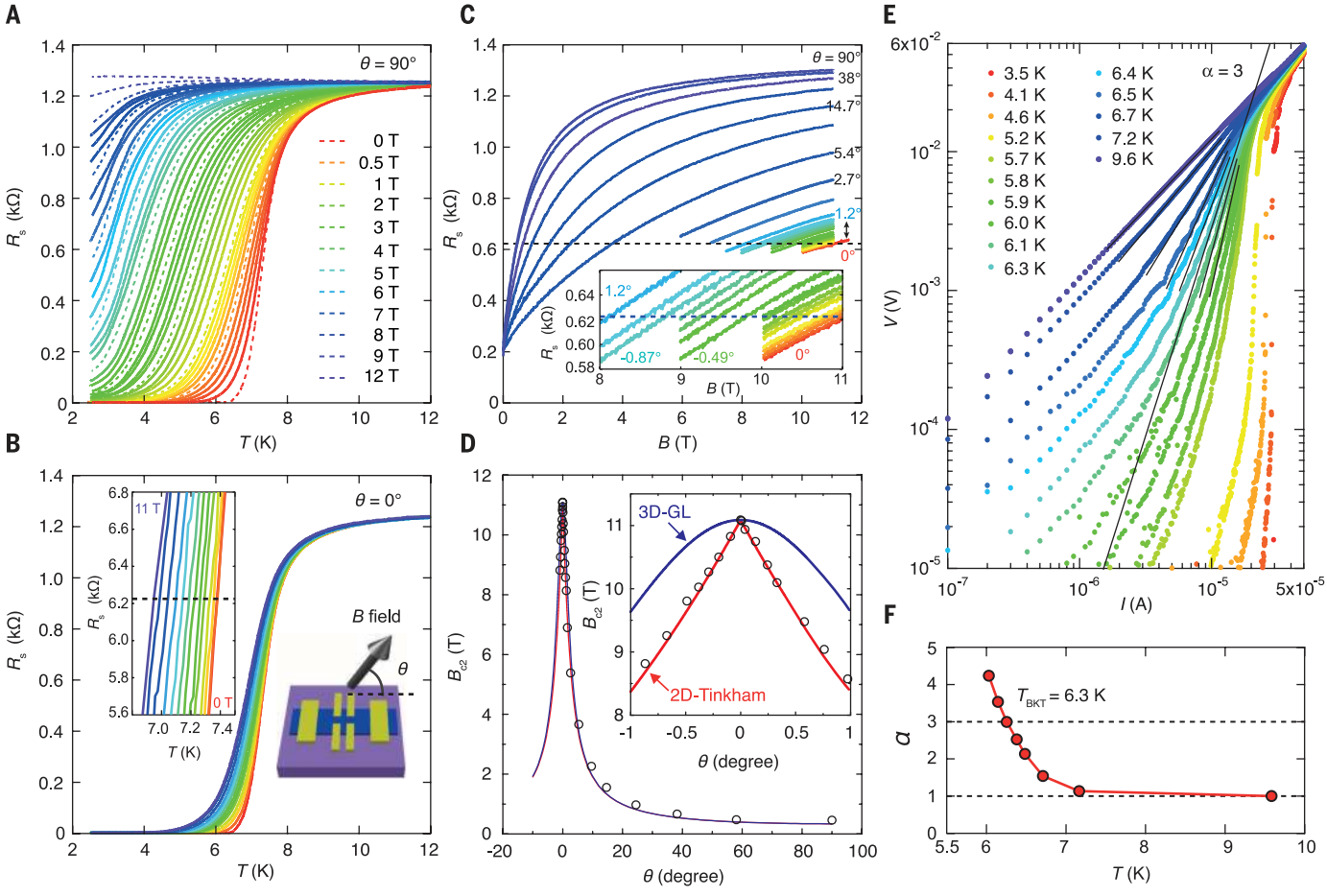

Fig. 2. 2D superconductivity in gated MoS_2 (sample D24). Temperature dependence of R_s under a constant out-of-plane (**A**) and in-plane (**B**) magnetic field, up to 12 T. In (B), the left inset shows a close-up view of the data near $R_N/2$ within 1 K. In the right inset, θ is the angle between the B field and the MoS_2 surface. (**C**) Angular dependence of R_s, where the dashed line denotes $R_s = R_N/2$. In the inset, the data are shown in detail within ±1° of the in-plane field configuration (θ = 0°). (**D**) Angular dependence of B_{c2}, which is fitted by both the 2D Tinkham model (red) and the 3D anisotropic GL model (blue). In the inset, the angular dependence of B_{c2} is shown in detail within ±1° of the in-plane field configuration (θ = 0°). (**E**) The V-I relationship at different temperatures close to T_c, plotted on a logarithmic scale. The black lines are fits close to metal-superconductor transitions. The long black line denotes $V \propto I^3$, which gives T_{BKT}. (**F**) Temperature dependence of α from fitting the power law dependence of $V \propto I^{\alpha}$ from the black lines in (E). T_{BKT} = 6.3 K is obtained for α = 3.

The charge distribution of our gated system implies that the superconducting state thus formed should exhibit a purely 2D nature. To demonstrate this dimensionality, we have characterized sample D24 [with $T_c(0)$ = 7.38 K] with a series of measurements. The temperature dependences of R_s under out-of- and in-plane magnetic fields (Fig. 2, A and B) are highly anisotropic. The angular dependence of B_{c2} at T = 6.99 K (Fig. 2D) was extracted from Fig. 2C. Curves fitted with the 2D Tinkham formula (red curve) (*30*) and the 3D anisotropic Ginzburg-Landau (GL) model (blue curve) (*2*) show that for $\theta > \pm 1°$ (where θ is the angle between the B field and the MoS_2 surface), the data are consistent with both models, whereas for $\theta < \pm 1°$ (Fig. 2D, inset), the cusp-shaped dependence can only be explained with a 2D model. These measurements show that our system exhibits 2D superconductivity, similar to $LaAlO_3$/$SrTiO_3$ interfaces (*31*) and ion-gated $SrTiO_3$ surfaces (*32*). From the voltage-current (*V-I*) dependence at different temperatures close to $T_c(0)$ (Fig. 2E), we determined that the Berezinskii-Kosterlitz-Thouless temperature T_{BKT} is 6.3 K for our 2D system (Fig. 2F). *V-I* characteristics in a magnetic field (fig. S3) exhibit similar critical behavior to the zero-field data, with their T_{BKT} values effectively reduced by increasing the magnetic field.

A moderate in-plane B field of up to 12 T shows little effect on the superconducting transition temperature [where $T_c(0)$ = 7.38 K and the Pauli limit B_P = 13.7 T (Fig. 2B)]; thus, the B_{c2} of the system must be far above B_P. To confirm this, we performed a high field measurement up to 37 T [section 2 of (*16*)] on sample D1 after observing a steep increase in B_{c2} near $T_c(0)$ = 5.5 K (Fig. 3C, green dots). By controlling the gating strength, superconducting states with $T_c(0)$ = 2.37 and 7.64 K were induced in sample D1. For $T_c(0)$ = 2.37 K, we obtained B_{c2} as the magnetic field required to reach 50% of the normal state resistivity (R_N) (Fig. 3A). B_{c2} is above 20 T at 1.46 K (Fig. 3C, red circles), which is more than four times the B_P. The data from the second gating [$T_c(0)$ = 7.64 K (Fig. 3B)] show only a weak reduction of T_c by ~1 K at even the highest magnetic field, 32.5 T (~ 2.3 × B_p).

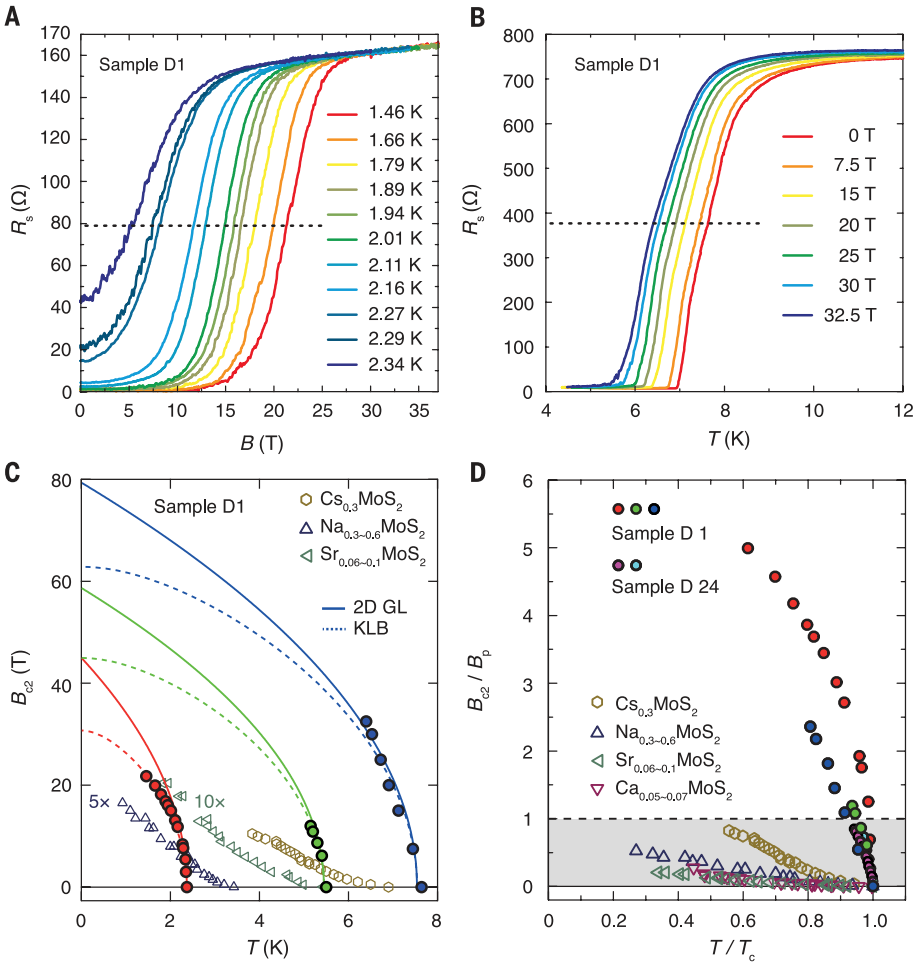

Fig. 3. Determining the in-plane upper critical field B_{c2} at different T_c (samples D1 and D24). (**A**) Magnetoresistance of sample D1 [with $T_c(0)$ = 2.37 K near the onset of the superconducting phase] as a function of an in-plane magnetic field up to 37 T, at various temperatures. (**B**) Temperature dependence of R_s for sample D1 [with $T_c(0)$ = 7.64 K] under different in-plane magnetic fields up to 32.5 T. The dashed lines in (A) and (B) indicate $R_N/2$. B_{c2} is determined as the intercept between dashed lines and R_s curves. (**C**) Temperature dependence of B_{c2} for superconducting states induced in sample D1 with different T_c [solid circles; colors follow (D)]. The B_{c2} for alkali metal–intercalated bulk MoS_2 compounds is from (*41*) and is shown for comparison. The B_{c2} for gate-induced states is fitted as a function of temperature using the 2D GL (solid line) and KLB (dashed line) models. (**D**) B_{c2} normalized by B_p, as a function of reduced temperature T/T_c, including superconducting states from alkali-doped bulk phases and gated-induced phases (samples D1 and D24). The dashed line denotes B_p and sets the boundary of the Pauli limited regime (shaded).

With controlling the gating strength, superconducting states with $T_c(0)$ = 2.37 and 7.64 K were induced in sample D1. For $T_c(0)$ = 2.37 K, we obtained B_{c2} as the magnetic field required to reach 50% of the normal state resistivity (R_N) (Fig. 3A). B_{c2} is above 20 T at 1.46 K (Fig. 3C, red circles), which is more than four times the B_P. The data from the second gating [$T_c(0)$ = 7.64 K (Fig. 3B)] show only a weak reduction of T_c by ~1 K at even the highest magnetic field, 32.5 T (~ 2.3 × B_p).

The temperature dependences of in-plane B_{c2} for sample D1 in three different states (Fig. 3C) are fitted using a phenomenological GL theory in the 2D limit (*2*) and the microscopic Klemm-Luther-Beasley (KLB) theory (*12*, *15*, *33*). The extrapolated zero-temperature in-plane B_{c2} is far beyond B_p for all three superconducting states. The zero-temperature B_{c2} predicted by 2D GL theory, without taking spin into account, is larger than that estimated by the KLB theory, which considers both the limiting effect from spin paramagnetism and the enhancing effect by the SOS from disorder. To fit the data using the KLB theory (dashed curves in Fig. 3C), the interlayer coupling has to be set to zero. This strongly suggests that the induced superconductivity is 2D, which is consistent with the conclusion drawn from Fig. 2 and previous theoretical calculations (*17*, *26*) and ARPES measurements (*27*, *28*) regarding predominant doping in the outermost layer. Curves fitted with the KLB theory yield a very short SOS time of ~24 fs (fig. S5), which is less than the total scattering time of 185 fs estimated from resistivity measurements at 15 K (table S2) and much shorter than the estimation of nanoseconds calculated for MoS_2 at the carrier density range accessed by this work (*34*). Short spin-orbit scattering times of ~40 to 50 fs have also been observed in organic molecule–intercalated TaS_2 (*35*–*37*), $(LaSe)_{1.14}(NbSe_2)$ (*38*, *39*), and the organic superconductor κ-$(ET)_4Hg_{2.89}Br_8$ [ET, bis(ethylenedithio)tetrathiafulvalene] (*40*).

The temperature dependence of B_{c2} in bulk superconducting MoS_2 intercalated by alkali metals (*41*) near $T_c(0)$ is linear instead of square root (Fig. 3C). The slight upturn of B_{c2} toward lower temperatures away from $T_c(0)$ is the evidence of crossover from 3D to 2D superconducting states (*12*, *33*, *36*–*38*) caused by the layered nature of the bulk crystal. In these bulk phases, the measured B_{c2} values are much smaller than or comparable (when Cs dopants are intercalated) to B_p (*41*).

This behavior is visualized in Fig. 3D, where the in-plane B_{c2} normalized by B_p for bulk superconducting phases falls within the shaded area bounded by the Pauli limit. In contrast, all gate-induced phases (from samples D1 and D24) are far above both B_p (dashed line) and bulk-phase B_{c2}. The D1 with $T_c(0)$ = 2.37 K, which is separated from the other gate-induced states, exhibits the largest enhancement. If the large SOS rate extracted from the KLB fitting (Fig. 3C) were the reason for the enhancement of B_{c2} in gate-induced phases, we would expect it to also enhance

B_{c2} in the bulk phases. The difference shown in Fig. 3D indicates that SOS is unlikely to be the origin of the enhancement of B_{c2} in the gated phases.

Excluding SOS as the principal mechanism for the strong enhancement of the in-plane B_{c2}, and taking into account recent developments in understanding the band structures of monolayer MoS_2 (*42*, *43*), we propose that this B_{c2} enhancement is mainly caused by the intrinsic spin-orbit coupling in MoS_2. Near the K points of the Brillouin zone (Fig. 1A) and on the basis of spin-up and -down electrons $[\psi_{k\uparrow}, \psi_{k\downarrow}]$, the normal-state Hamiltonian of monolayer MoS_2 in the presence of an external field can be described by (*24*)

$$H(\mathbf{k}+\epsilon\mathbf{K}) = \varepsilon_k + \epsilon\beta_{so}\sigma_z + \alpha_R \mathbf{g}_F \cdot \sigma + \mathbf{b}\cdot\sigma \quad (1)$$

Here, $\varepsilon_k = \frac{\mathbf{k}^2}{2m} - \mu$ denotes the kinetic energy with chemical potential μ; $\mathbf{k} = (k_x, k_y, 0)$ is the kinetic momentum of electrons in the K and K' valleys; $\mathbf{K}$ is the kinetic momentum of the K valley; m is the effective mass of the electrons; $\sigma = (\sigma_x, \sigma_y, \sigma_z)$ are the Pauli matrices; $\mathbf{g}_F = (k_y, -k_x, 0)$ denotes the Rashba vector (lying in-plane); α_R and β_{SO} are the strength of Rashba and intrinsic SOC, respectively; $\epsilon = \pm 1$ is the valley index (1 at the K valley and −1 at the K' valley); and $\mathbf{b} = \mu_B\mathbf{B}$ is the external Zeeman field (where μ_B is the Bohr magneton). The intrinsic SOC term $\epsilon\beta_{SO}\sigma_z$, due to in-plane inversion symmetry breaking, induces an effective magnetic field pointing out of the plane (z direction), which has opposite signs at opposite valleys (green arrows in Fig. 1A). This Zeeman-like effective magnetic field $\mathbf{B}_{eff} = \epsilon\beta_{SO}\hat{z}/g\mu_B$ (g, gyromagnetic ratio; $\hat{z}$, unit vector in the out-of-plane direction) will only appear in our multilayered system after applying a strong electric field, which isolates the outermost layers from the other layers (*17*, *44*), thus mimicking a monolayer system. The large electric field generated by gating reaches ~50 million volts/cm (*17*) in our system, causing additional out-of-plane inversion symmetry breaking and creating a Rashba-type effective magnetic field $\mathbf{B}_{Ra} = \alpha_R\mathbf{g}_F/g\mu_B$.

The total energy in a magnetic field is schematically shown in Fig. 4, A to D. If the electron spin aligned by $\mathbf{B}_{eff}$ ($\mathbf{B}_{Ra}$) stays parallel to the external magnetic field $\mathbf{B}_{ex}$ (Fig. 4, A and C), the system gains energy through coupling between spin and external fields as $\mu_B\mathbf{B}_{ex}$. Therefore, B_{c2} is limited by B_p (Fig. 4A), or it can reach $\sqrt{2}\,B_p$ (Fig. 4C) when coupling is reduced in a Rashba-type spin configuration (*10*). When $\mathbf{B}_{eff}$ and $\mathbf{B}_{Ra}$ are perpendicular to $\mathbf{B}_{ex}$, as respectively shown in Fig. 4, B and D, the spin aligned by both effective fields is orthogonal to $\mathbf{B}_{ex}$. Hence, the coupling between spin and $\mathbf{B}_{ex}$ is minimized, and B_{c2} can easily surpass B_p in these two cases.

To theoretically describe our system when subjected to an in-plane external magnetic field (combining the cases shown in Fig. 4, B and

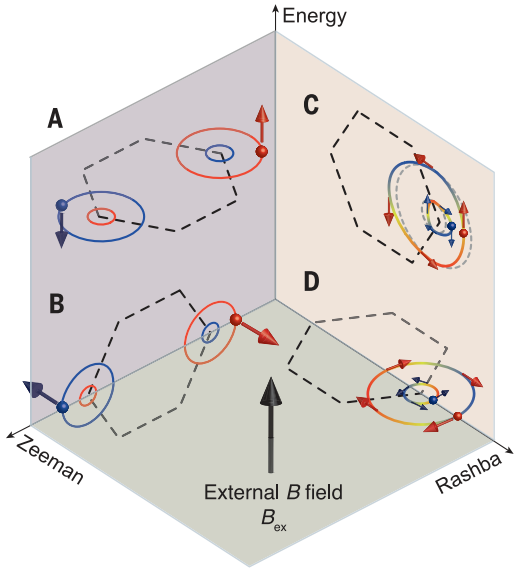

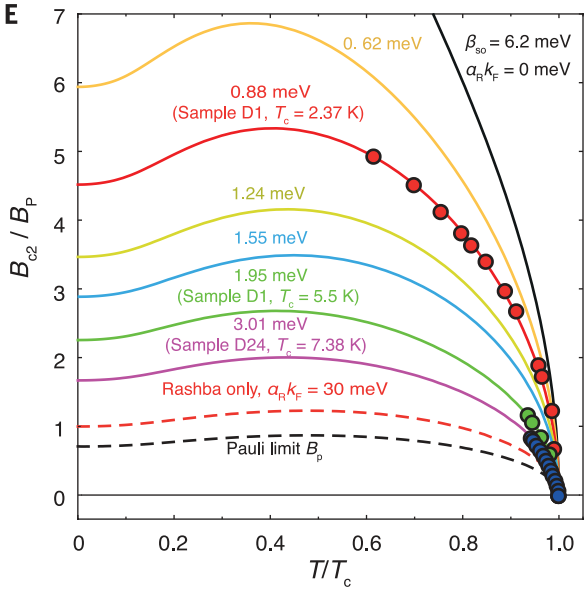

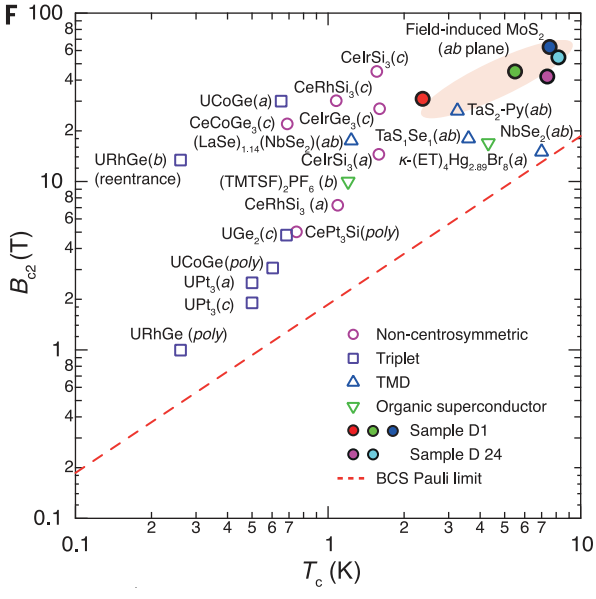

Fig. 4. Interplay between an external magnetic field and the spins of Cooper pairs aligned by Zeeman and Rashba-type effective magnetic fields. (**A** to **D**) Illustration of the acquisition of Zeeman energy through coupling between an external magnetic field and the spins of Cooper pairs formed near the K and K' points of the Brillouin zone (not to scale). When Rashba or Zeeman SOC aligns the spins of Cooper pairs parallel to the external field, the increase in Zeeman energy due to parallel coupling between the field and the spin eventually can cause the pair to break [(A) and (C)]. In (B) and (D), the acquired Zeeman energy is minimized as a result of the orthogonal coupling between the field and the aligned spins, which effectively protects the Cooper pairs from depairing. (**E**) Theoretical fitting of the relationship between B_{c2}/B_p and T/T_c for samples D1 [$T_c(0)$ = 2.37 K and 5.5 K] and D24 [$T_c(0)$ = 7.38 K], using a fixed effective Zeeman field (β_{SO} = 6.2 meV) and an increasing Rashba field ($\alpha_R k_F$ ranges from 10 to ~50% of β_{SO}) [section 6 of (*16*)]. Two dashed lines show the special cases calculated by equation S3, when only the Rashba field ($\alpha_R k_F$ = 30 meV; β_{SO} = 0) is considered (red), and when both the Zeeman and Rashba fields are zero (black). In the former case, a large $\alpha_R k_F$ causes a moderate increase of B_{c2} to ~$\sqrt{2}B_p$ (*10*). In the latter case, the conventional Pauli limit at zero temperature is recovered. (**F**) Plot of B_{c2} versus T_c for different superconductors [a magnetic field was applied along crystal axes *a*, *b*, or *c* or to a polycrystalline (*poly*)]. The data shown are from well-known systems including noncentrosymmetric (pink circles), triplet (purple squares) (*6*, *8*, *9*), low-dimensional organic (green triangles) (*40*, *50*–*52*), and bulk TMD superconductors (blue triangles) (*35*–*38*, *47*). The robustness of the spin protection can be measured by the vertical distance between B_{c2} and the red dashed line denoting B_p. Gate-induced superconductivity from samples D1 and D24 are among the states with the highest B_{c2}/B_p ratio. In $(LaSe)_{1.14}(NbSe_2)$, T_c was determined at 95% of R_N; T_c in organic molecule–intercalated TMDs was obtained by extrapolating to zero resistance; and all other systems use the standard of 50% of R_N.

C), we introduced the pairing potential terms $\Delta\psi_{k\uparrow}\psi_{-k\downarrow} + h.c.$ into $H(\mathbf{k})$ and solved the self-consistent mean field gap equation [section 6 of (*16*); *h.c.*, hermitian conjugate]. The in-plane B_{c2} for a sample with a given T_c can then be determined by including the intrinsic SOC term β_{SO} and the Rashba energy $\alpha_R k_F$, where k_F is the Fermi momentum.

For the most extensive data set from sample D1 [$T_c(0)$ = 2.37 K], the relationship between B_{c2}/B_p and the reduced temperature T/T_c, shown in Fig. 4E, can be fitted well with β_{SO} = 6.2 meV and $\alpha_R k_F$ = 0.88 meV. The value obtained for β_{SO} corresponds to an out-of-plane field of ~114 T, which is comparable to the value expected from theoretical calculation at the *K* point (3 meV) (*23*). The Rashba energy obtained can be regarded as an upper bound, because the present model does not include impurity scattering, which can also reduce B_{c2} (*45*).

The scale of B_{c2} enhancement is determined by a destructive interplay between intrinsic β_{SO} and $\alpha_R k_F$. Reaching higher $T_c(0)$ requires stronger doping under higher electric fields, with a concomitant increase of $\mathbf{B}_{Ra}$. As a result of this competition, the in-plane B_{c2} protection should be weakened with the increase of $T_c(0)$. To support this argument, we chose two other superconducting samples that showed consecutively higher $T_c(0)$ (from D1 and D24). By assuming identical β_{SO} (6.2 meV), B_{c2} from D1 with $T_c(0)$ = 5.5 K and B_{c2} from D24 with $T_c(0)$ = 7.38 K can be well fitted using $\alpha_R k_F$ = 1.94 and 3.02 meV, respectively; these values are consistent with the expected increase of $\alpha_R k_F$ with $T_c(0)$ (Fig. 4E).

The effective Zeeman field and its orthogonal protection in individual layers can also be induced by reducing the interlayer coupling in bulk superconducting TMDs (*33*, *35*, *38*, *46*, *47*). Therefore, a large in-plane B_{c2} was also observed in bulk when lattice symmetry was lowered by intercalating organic molecules and alkali elements with large radii (Cs-intercalated MoS_2 shows the highest B_{c2} among bulk phases in Fig. 3D) or by forming a charge density wave (*46*).

We compared our B_{c2} results with those obtained from other superconductors with enhanced B_{c2} under their maximum spin protection along the labeled crystal axis (Fig. 4F); we found that the Zeeman field–protected states in our samples are among the states that are most robust against external magnetic fields. Given the very similar band structures found in 2*H*-type TMDs with universal Zeeman-type spin splitting and the recent successes in inducing more TMD superconductors using the field effect (*17*, *48*, *49*), we would expect a family of Ising superconductors in 2*H*-type TMDs. The concept of the Ising superconductor is also applicable to other layered systems, where similar intrinsic SOC could be induced by symmetry breaking.

REFERENCES AND NOTES

1. G. R. Stewart, *Rev. Mod. Phys.* **56**, 755–787 (1984).
2. M. Tinkham, *Introduction to Superconductivity* (McGraw-Hill, 1996).
3. A. M. Clogston, *Phys. Rev. Lett.* **9**, 266–267 (1962).
4. B. S. Chandrasekhar, *Appl. Phys. Lett.* **1**, 7 (1962).
5. Y. Matsuda, H. Shimahara, *J. Phys. Soc. Jpn.* **76**, 051005 (2007).
6. D. Aoki *et al.*, *Nature* **413**, 613–616 (2001).
7. N. T. Huy *et al.*, *Phys. Rev. Lett.* **99**, 067006 (2007).
8. D. Aoki, J. Flouquet, *J. Phys. Soc. Jpn.* **81**, 011003 (2012).
9. E. Bauer, M. Sigrist, Eds., *Non-Centrosymmetric Superconductors* (Springer-Verlag, 2012).
10. L. P. Gor'kov, E. I. Rashba, *Phys. Rev. Lett.* **87**, 037004 (2001).
11. A. A. Abrikosov, L. P. Gor'kov, *Sov. Phys. JETP* **15**, 752 (1962).
12. R. A. Klemm, A. Luther, M. R. Beasley, *Phys. Rev. B* **12**, 877–891 (1975).
13. P. M. Tedrow, R. Meservey, *Phys. Rev. B* **25**, 171–178 (1982).
14. X. S. Wu, P. W. Adams, Y. Yang, R. L. McCarley, *Phys. Rev. Lett.* **96**, 127002 (2006).
15. R. A. Klemm, *Layered Superconductors: Volume 1* (International Series of Monographs on Physics 153, Oxford Univ. Press, 2011).
16. Materials and methods are available as supplementary materials on *Science* Online.
17. J. T. Ye *et al.*, *Science* **338**, 1193–1196 (2012).
18. K. Ueno *et al.*, *Nat. Mater.* **7**, 855–858 (2008).
19. H. Yuan *et al.*, *Adv. Funct. Mater.* **19**, 1046–1053 (2009).
20. J. T. Ye *et al.*, *Nat. Mater.* **9**, 125–128 (2010).
21. K. Ueno *et al.*, *Nat. Nanotechnol.* **6**, 408–412 (2011).
22. J. Ye *et al.*, *Proc. Natl. Acad. Sci. U.S.A.* **108**, 13002–13006 (2011).
23. A. Kormányos *et al.*, *Phys. Rev. B* **88**, 045416 (2013).
24. N. F. Q. Yuan, K. F. Mak, K. T. Law, *Phys. Rev. Lett.* **113**, 097001 (2014).
25. M. Rösner, S. Haas, T. O. Wehling, *Phys. Rev. B* **90**, 245105 (2014).
26. R. Roldán, E. Cappelluti, F. Guinea, *Phys. Rev. B* **88**, 054515 (2013).
27. T. Eknapakul *et al.*, *Nano Lett.* **14**, 1312–1316 (2014).
28. Y. Zhang *et al.*, *Nat. Nanotechnol.* **9**, 111–115 (2014).
29. Y. Ge, A. Y. Liu, *Phys. Rev. B* **87**, 241408 (2013).
30. M. Tinkham, *Phys. Rev.* **129**, 2413–2422 (1963).
31. N. Reyren *et al.*, *Appl. Phys. Lett.* **94**, 112506 (2009).
32. K. Ueno *et al.*, *Phys. Rev. B* **89**, 020508 (2014).
33. R. A. Klemm, *Physica C* **514**, 86–94 (2015).
34. L. Wang, M. W. Wu, *Phys. Lett. A* **378**, 1336–1340 (2014).
35. R. C. Morris, R. V. Coleman, *Phys. Rev. B* **7**, 991–1001 (1973).
36. R. V. Coleman, G. K. Eiserman, S. J. Hillenius, A. T. Mitchell, J. L. Vicent, *Phys. Rev. B* **27**, 125–139 (1983).
37. D. E. Prober, R. E. Schwall, M. R. Beasley, *Phys. Rev. B* **21**, 2717–2733 (1980).
38. P. Samuely *et al.*, *Physica C* **369**, 61–67 (2002).
39. J. Kačmarčík *et al.*, *Physica C* **468**, 543–546 (2008).
40. R. N. Lyubovskaya, R. B. Lyubovskii, M. K. Kakova, S. I. Pesotskii, *JETP Lett.* **51**, 361 (1990).
41. J. A. Woollam, R. B. Somoano, *Phys. Rev. B* **13**, 3843–3853 (1976).
42. D. Xiao, G.-B. Liu, W. Feng, X. Xu, W. Yao, *Phys. Rev. Lett.* **108**, 196802 (2012).
43. Z. Y. Zhu, Y. C. Cheng, U. Schwingenschlögl, *Phys. Rev. B* **84**, 153402 (2011).
44. H. Yuan *et al.*, *Nat. Phys.* **9**, 563–569 (2013).
45. L. N. Bulaevskii, A. A. Guseinov, A. I. Rusinov, *Sov. Phys. JETP* **44**, 1243 (1976).
46. S. Foner, E. J. McNiff Jr., *Phys. Lett. A* **45**, 429–430 (1973).
47. Y. Kashihara, A. Nishida, H. Yoshioka, *J. Phys. Soc. Jpn.* **46**, 1112–1118 (1979).
48. K. Taniguchi, A. Matsumoto, H. Shimotani, H. Takagi, *Appl. Phys. Lett.* **101**, 042603 (2012).
49. W. Shi *et al.*, *Sci. Rep.* **5**, 12534 (2015).
50. I. J. Lee, M. J. Naughton, G. M. Danner, P. M. Chaikin, *Phys. Rev. Lett.* **78**, 3555–3558 (1997).
51. I. J. Lee, P. M. Chaikin, M. J. Naughton, *Phys. Rev. B* **62**, R14669–R14672 (2000).
52. P. M. Chaikin, E. I. Chashechkina, I. J. Lee, M. J. Naughton, *J. Phys. Condens. Matter* **10**, 11301–11314 (1998).

ACKNOWLEDGMENTS

We acknowledge support from the High Field Magnet Laboratory Nijmegen (HFML-RU/FOM), a member of the European Magnetic Field Laboratory. J.T.Y. acknowledges funding from the European Research Council (consolidator grant no. 648855 lg-QPD). U.Z. was supported by the DESCO program (2-Dimensional Electron Systems in Complex Oxides, program no. 149) of the Foundation for Fundamental Research on Matter, which is part of the Netherlands Organization for Scientific Research. K.T.L. and N.F.Q.Y. were supported by the Hong Kong Research Grants Council and the Croucher Foundation through grants HKUST3/CRF/13G, 602813, 605512, and 16303014 and an Innovation Grant.

SUPPLEMENTARY MATERIALS

www.sciencemag.org/content/350/6266/1353/suppl/DC1
Materials and Methods
Figs. S1 to S5
Tables S1 and S2
References (*53*–*65*)

30 March 2015; accepted 21 October 2015
Published online 12 November 2015
10.1126/science.aab2277

ICE SHEETS

Fast retreat of Zachariæ Isstrøm, northeast Greenland

J. Mouginot,[1]* E. Rignot,[1,2] B. Scheuchl,[1] I. Fenty,[2] A. Khazendar,[2] M. Morlighem,[1] A. Buzzi,[1] J. Paden[3]

After 8 years of decay of its ice shelf, Zachariæ Isstrøm, a major glacier of northeast Greenland that holds a 0.5-meter sea-level rise equivalent, entered a phase of accelerated retreat in fall 2012. The acceleration rate of its ice velocity tripled, melting of its residual ice shelf and thinning of its grounded portion doubled, and calving is now occurring at its grounding line. Warmer air and ocean temperatures have caused the glacier to detach from a stabilizing sill and retreat rapidly along a downward-sloping, marine-based bed. Its equal-ice-volume neighbor, Nioghalvfjerdsfjorden, is also melting rapidly but retreating slowly along an upward-sloping bed. The destabilization of this marine-based sector will increase sea-level rise from the Greenland Ice Sheet for decades to come.

Zachariæ Isstrøm (ZI) and Nioghalvfjerdsfjorden glacier (NG), in northeast Greenland, drain a sector 198,380 km^2 in size, or 12% of the Greenland Ice Sheet (*1*). These two glaciers together drain the northeast Greenland ice stream, the only large, dynamic feature that extends continuously deep to the ice sheet interior near Greenland's summit (*2*). This marine-based sector holds a 1.1-m sea-level rise equivalent (*3*) (Fig. 1D).

We constructed a high-resolution bed topography of both glaciers (Fig. 1) using a mass conservation method over grounded ice (*3*) and airborne gravity inversion (*4*) over floating ice.